Remarkable Topological Features of Electronic Band Dispersion of IrGa and RhGa Compounds from First Principles

Jean P. Alvarez,[1, a)] David Gordon,[1, b)] Jack Howard,[2, c)] Joshua Steier,[2, d)] Kalani Hettiarachchilage,[3, e)] and Neel Haldolaarachchige[1, f)]

[1)]*Department of Physical Science, Bergen Community College, Paramus, New Jersey 07652, USA*
[2)]*Department of Physics, Seton Hall University, South Orange, New Jersey 07079, USA*
[3)]*Department of Physics and Astronomy, College of Staten Island, 2800 Victory Blvd., Staten Island, New York 10314, USA*

[a)]*Corresponding author: jpa113@rutgers.edu*
[b)]*gordo.1025@gmail.com*
[c)]*jack.howard@student.shu.edu*
[d)]*joshua.steier@stonybrook.edu*
[e)]*kalani.hettiarachchilage@shu.edu*
[f)]*nhaldolaarachchige@bergen.edu*

Abstract. Exotic behavior of linearly dispersed electronic bands near the Fermi level implies advanced physical properties in a material. In this paper, we present an *ab initio* study of the electronic properties of *IrGa* and *RhGa*, with and without spin-orbit interaction, using first-principles calculations. Linearly dispersed band crossings, reminiscent of topological semimetallic band structures, were identified near the Fermi energy. These include type-I and type-II Dirac points and nodal lines. By applying compressive and tensile stress to the lattice along x, y, and z, the response to the band structure near the Fermi level has been studied.

INTRODUCTION

The field of topological matter is currently one of the most active, and hence discovering new exciting topological materials is of interest. Among topological materials, topological insulators and semimetals are classified as topological if nontrivial Chern numbers or Berry phases can be detected. Just as with normal insulating materials, topological insulators have an energy gap between the valence and conduction bands, but they exhibit gapless, conducting states on the surface [1, 2]. Topological semimetals are categorized mainly into three types: Dirac semimetals, Weyl semimetals, and nodal line semimetals. In all these topological semimetals, bands cross in momentum space and are inverted beyond the crossing point (or line) [3]. Weyl and Dirac semimetals exhibit band crossing points, while in nodal line semimetals the bands are degenerate along a 1D nodal line or loop. Nodal line semimetals can be the origin of many different topological phases; spin-orbit coupling can gap to a nodal line, Weyl points, Dirac points, or to a topological insulating phase, depending on the crystal symmetry. For example, to have a Weyl semimetal, either inversion or time-reversal symmetry needs to be broken [4, 5].

Dirac materials have a linear or quasilinear band dispersion (Dirac bands) near the Fermi energy, which is ineffable within the nonrelativistic Schrödinger description but can be described by the Dirac equation by considering massless high-mobility electrons. Such a Dirac band dispersion was first predicted in graphene [6, 7], which exhibits six Dirac points. The linear crossing point at the Fermi level in graphene has been linked to its electronic and optical properties. After the discovery of graphene, the search for Dirac materials was extended to 3D materials [8,9,10]. Dirac semimetal behavior was first predicted and then realized in Na_3Bi and Cd_3As_2 [8,14-20,47], Weyl semimetal behavior was predicted and realized in TaAs [32, 41-46], and nodal line semimetal behavior was predicted in Cu_3PdN, Ca_3P2, CaP_3, PbO_2, CaAg, TiB_2, CaAgAs, ZrB_2, $SrSi_2$, LaSiS [9,23-31] and experimentally realized in $PbTaSe_2$, $PtSn_4$, ZrSiS, ZrSiSe, ZrSiTe, HfSiS, and ZrSnTe [32-40]. Linear band crossing points can be classified into two categories by considering the slope of the band dispersion at the crossing point. Type-I Dirac points are "upright" in respect to energy, while type-II Dirac points are tilted, thus having unequal slopes of the band dispersions. These two types differ in their density of states at the Fermi level, which vanishes for type-I Dirac nodes but is finite for type-II nodes [11-13]. In general, first-principles electronic structure calculations based on density functional theory (DFT) play an important role in exploring topological electronic materials theoretically.

In this work, a detailed study of the electronic band structure and density of states of iridium gallium (*IrGa*) [53, 54], and rhodium gallium (*RhGa*) is presented and their topological nature is reported. To the best of our knowledge, these compounds have not yet been discussed in detail for their topological behaviors. In this paper, we report

calculated electronic structures of *IrGa* and *RhGa*, and predict that both compounds exhibit topological features. The same features are observed in both compounds; hence we mainly present the detailed study of *IrGa*. In the *IrGa* bulk band structure there are highly dispersive bands that cross the Fermi level. Without the SO effect, a nodal line formed by the highly dispersive bands is located near the Fermi level around the R point. The nodal line is protected in the absence of SO and is gapped due to SO coupling. Along M-R, there is a type-1 Dirac crossing. A flat band can be seen along M-R near the Fermi level that crosses the linear bands twice and gaps out with SO coupling. Additionally, the pressure effect of the material was tested.

CRYSTAL STRUCTURE AND COMPUTATIONAL METHOD

Electron configurations of *Ir*, *Rh*, and *Ga* are $[Xe]4f^{14}5d^{7}6s^{2}$, $[Kr]4d^{8}5s^{1}$, and $[Ar]3d^{10}4s^{2}4p^{1}$, respectively. The *Ir*(*Rh*)-d orbitals and *Rh*-s orbitals are not fully occupied, whereas *Ga*-p orbitals are not fully occupied. Both are intermetallic compounds with a cubic lattice structure. The lattice parameters of *IrGa* and *RhGa* are 3.0040 and 3.0034, respectively, [55] with the same space group symmetry of 221 (Pm-3m). The crystal is symmorphic in that it has both time-reversal and inversion symmetry. The optimized lattice parameter for *IrGa* is calculated by using volume optimization as a = 3.0566 and is used for all the calculations. It is comparable to the reported lattice parameter in Refs. [53,54]. Figure 1 shows the primitive cell structure of *IrGa*, the same as the conventional cell. The *Ga* atoms sit at the corners of the primitive cell, and *Ir* (*Rh*) atom is at the center of the primitive cell. The first Brillouin zone (BZ) of the structure is shown in the right panel of Fig. 1 with the high symmetry points on the cubic BZ and the Γ(0, 0, 0) point located at the center.

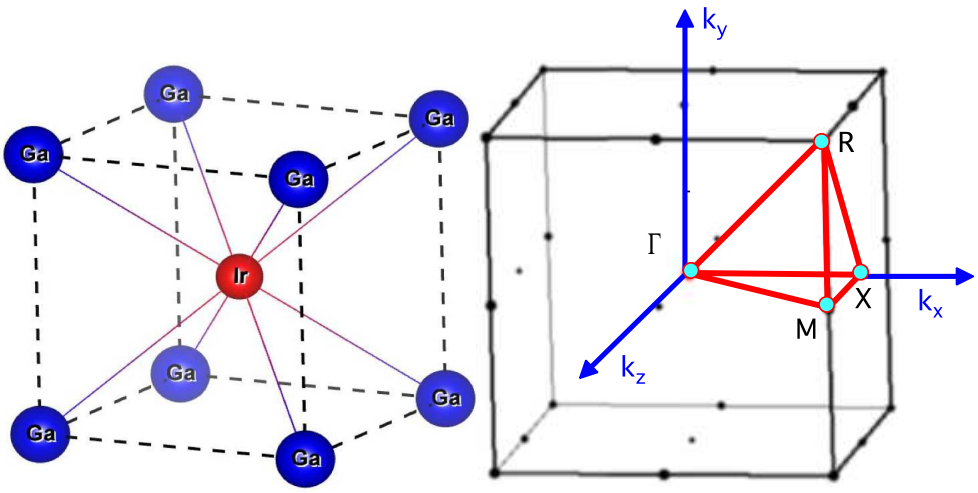

(a) (b)

FIGURE 1. Structure of bulk *IrGa*. Panel (a): The primitive unit cell. The blue spheres denote the *Ga* atoms and the red sphere is the *Ir* atom. Panel (b): Bulk primitive BZ. The k_x, k_y and k_z show the reciprocal lattice vectors. The light blue dots display the high symmetry points of the BZ with labeling Γ, R, X, and M.

The band structure and density of states were calculated by performing first-principal density functional theory (DFT) methods in the WEIN2K simulation package using the Perdew-Burke-Ernzerhof (PBE) pseudopotentials and the plane-wave basis set with the generalized gradient approximation (GGA) [56-60]. The BZ was sampled by using 20,000 k-points and setting the plane-wave cut-off parameters, RKmax, to 7 with extreme convergent of energy and charge. Calculations were performed with and without spin-orbit (SO) coupling. Volume optimization was performed to calculate the lattice parameters to corresponding pressures. The crystal momentum in units of $k = (\pi/a, \pi/a, \pi/a)$ is used throughout the discussion unless otherwise specified.

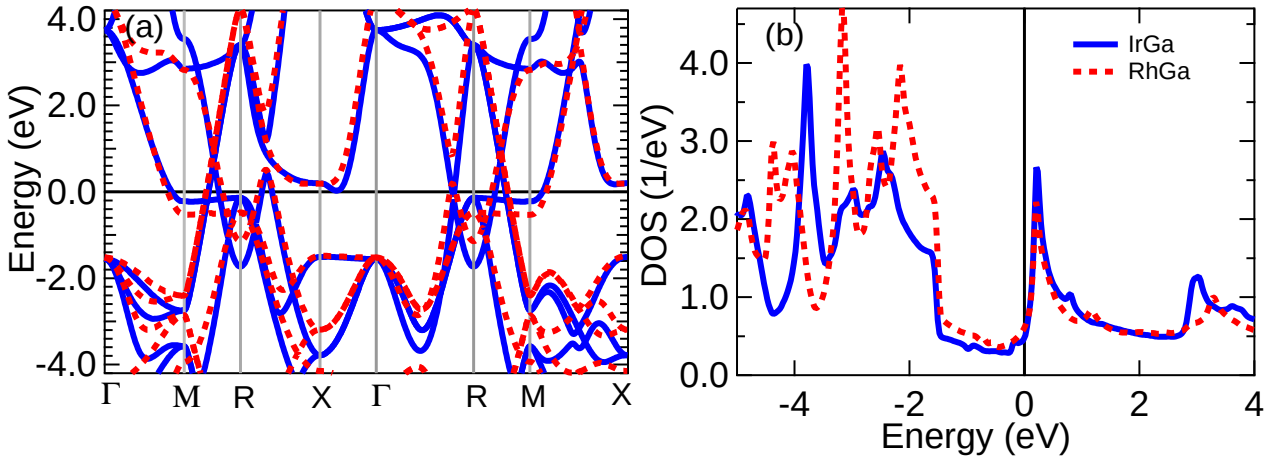

(a) (b)

FIGURE 2. Calculated electronic band structure and total density of states (DOS) for *IrGa* and *RhGa* compounds without SO coupling. (a): Calculated bulk band structures along the high-symmetry lines on the BZ k-path Γ-M-R-X-Γ-R-M-X shown in Fig. 1(b) for *IrGa* (blue solid lines) and *RhGa* (red dotted line). (b): The total DOS of *IrGa* is shown by the blue solid line, whereas the red dotted line shows the total DOS for the *RhGa* compound. The solid black line at zero indicates the Fermi level.

RESULTS AND DISCUSSION

The band structure calculations of *IrGa* and *RhGa* within GGA without inclusion of the SO coupling along the high-symmetry k-path Γ-M-R-X-Γ-R-M-X are plotted by setting the Fermi level to 0 eV on the energy scale, as shown in Fig. 2. The band structures of *IrGa* and *RhGa* are shown in Fig. 2(a) using blue solid lines and red dotted lines, respectively. The features of both band structures are the same. Total DOS calculations for *IrGa* and *RhGa* are shown in Fig. 2(b) by taking the blue solid and red dotted lines discretely. There are no measurable differences in the total DOS either. Due to these similarities, we extend the detailed study by choosing the *IrGa* compound.

The band structures of *IrGa* within GGA without inclusion of the SO coupling along the high-symmetry k-path Γ-M-R-X-Γ-R-M-X are plotted in Fig. 3. The left panel (a) shows the band structure of the *IrGa* compound, and the right panel (b) shows the atom-projected DOS calculation. There are few bands near the Fermi level. There is a single band that crosses the Fermi level near point M (shown in the Γ-M and M-X planes), and it was identified as the *Ir*-deg orbital. The range of linearly dispersed bands is large, and linear crossing of bands near the Fermi level is observed and discussed below. The results of the total and atom-projected DOS of *IrGa* help to elaborate on the nature of the bands near the Fermi level and provide information about the origin of the bands and contributions from each atom and each orbital to DOS. According to the results shown in the right panel (b) of Fig. 3, DOS near the Fermi level is very small (essentially a zero DOS at the Fermi level for perfect Dirac semimetals) and is mostly a contribution from the *Ir* atom, which is dominated by d-orbitals, while the contribution from *Ga* is very small. Since the SO couplings can be used to identify exotic band behaviors of Dirac materials, we perform an SO calculation for the *IrGa* system as shown in the bottom part of Fig. 3. The left panel (c) of the figure shows the SO calculation of the band structure which has more degenerated bands and opening gaps corresponding to the absence of SO coupling as discussed below. The right panel (d) of the figure represents the DOS contribution from each atom. When compared to the DOS without inclusion of the SO effect, there is no change in the DOS with SO coupling at the Fermi level, although the DOS near the Fermi surface displays sharp contrast.

Within the chosen k path there are band crossings in the M-R ($k_x = -\pi/a$, $k_z = -\pi/a$) plane near the Fermi level as enumerated from 1-3. Since irreducible representation (symmorphic crystal symmetries) allows us to access each eigenvalue along the chosen k-path, we can see connecting lines of bands and the same colored bands with the same symmetry. A zoomed-in picture of the irreducible representation of the M-R plane is displayed in the left panel of Fig. 4. It is very clear that bin 1 in Fig. 4 is a type-I twofold-degenerate Dirac point located at an energy of about 0.65 eV with the coordinates $(-0.55342, 0.28948, -0.55342)$. The linear crossing of the black line (irreducible representations of Γ_1 and Γ_5 of space group C_{4v}) is dominated by hybridized bands of *Ir*-dt2g and the *Ga*-s orbital.

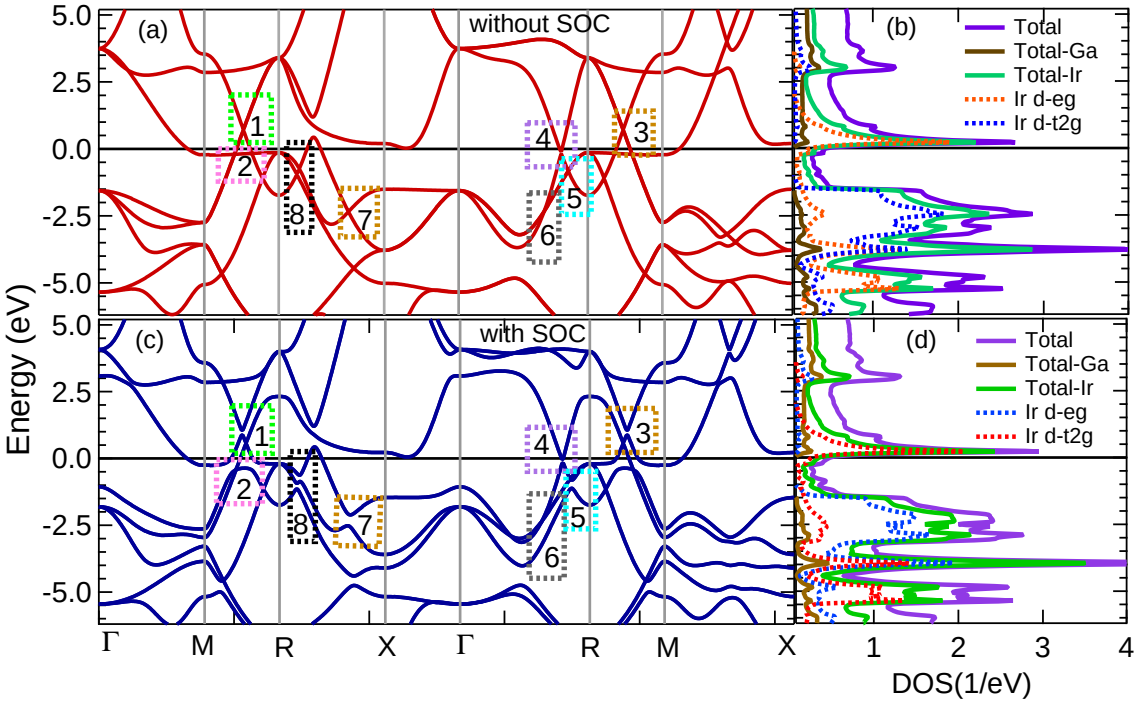

FIGURE 3. Calculated electronic band structure and atom-projected DOS for *IrGa* with and without SO coupling (SOC). Panel (a): Calculated bulk band structures along the high-symmetry k-path Γ-M-R-X-Γ-R-M-X shown in Fig. 1(b). The numbers from 1 to 8 are discussed in the content. Panel (b): The purple solid line denotes the total density of states of *IrGa*. The maximum contribution to the DOS comes from d orbitals of the *Ir* atoms as shown in the red and blue dotted lines, while *Ga* atoms contribute a small percentage as indicated with the solid brown line. The maximum contribution to the total DOS at the Fermi level forms from deg orbitals of the *Ir* atom. Panel (c): Calculated bulk band structures along the high-symmetry k-path as in the top panel but with SO coupling. Panel (d): The purple solid line denotes the DOS of *IrGa*. The maximum contribution to the DOS comes from d orbitals of the *Ir* atoms as denoted by the red and blue dotted lines, while *Ga* atoms contribute a small percentage as displayed by the solid brown line. The solid black line in all figures at zero indicates the Fermi level.

The gray line (Γ_5 of space group C_{4v}) is dominated by hybridized bands of *Ir*-dt2g, p, and *Ga*-p orbitals. The black and gray lines at the crossing point display the same and opposite slopes around ±16 eV. In the presence of SO coupling, the crossing point is fully gapped into threefold degeneracy with band inversion as shown in the right panel of Fig. 4. In conclusion, the crossing point is predicted to be a Dirac point protected by the absence of SO coupling with a predicted electron velocity of around 2.4×10^{16} /s calculated by $(1/\hbar)dE/dk$, which is similar to the experimentally measured velocity of Cd_3As_2 [20]. A flat energy dispersion of electrons at the Fermi level of a material leads to instabilities in the electronic system and can be claimed as a phase transition [63-65]. Within the chosen k path in the M-R plane ($k_x = -\pi/a$, $k_z = -\pi/a$) near the Fermi level, a flat band was predicted in -0.20 eV as enumerated in box 2 in the left panel of Fig. 4 without the SO effect. Although we predict a flat band, there is no singularity present in the DOS as expected to be in a phase transition [65]. With switching on SO coupling, the two crossings at the coordinates $(-0.55342, 0.29799, -0.55342)$ and $(-0.55342, 0.34907 - 0.55342)$ are gapped out into twofold degeneracy of each as displayed in the right panel of Fig. 4. In irreducible representation the first coordinate consists with Γ_1, Γ_2, and Γ_5 symmetries and the second coordinate consists with Γ_1 and Γ_2 that are protected by space group symmetry C_{4v}. The flat band is identified as *Ir*-deg orbitals. It is observed that the bands are linear and gap out with the SO effect, and the flat band has almost zero slope, while the other bands have around ±16 eV. By observation of the tilting of the bands, we predict that to be a type-II nodal line which transitions from a nodal line semimetal to a topological insulator in the presence of the SO effect. Similar single crossing of such a flat band has been discussed in $ScPd_3$ [62].

Additionally, a crossing at the coordinates $(-0.55342, 0.43422, -0.55342)$ represented by the Γ_1 and Γ_4 bands with energy -1.0 eV is protected by the C_{4v} space group symmetry. Bin 3 in the M-R plane represents this crossing, and it opens a small gap (twofold degeneracy) due to the SO effect, which is a nodal line formed around the R point.

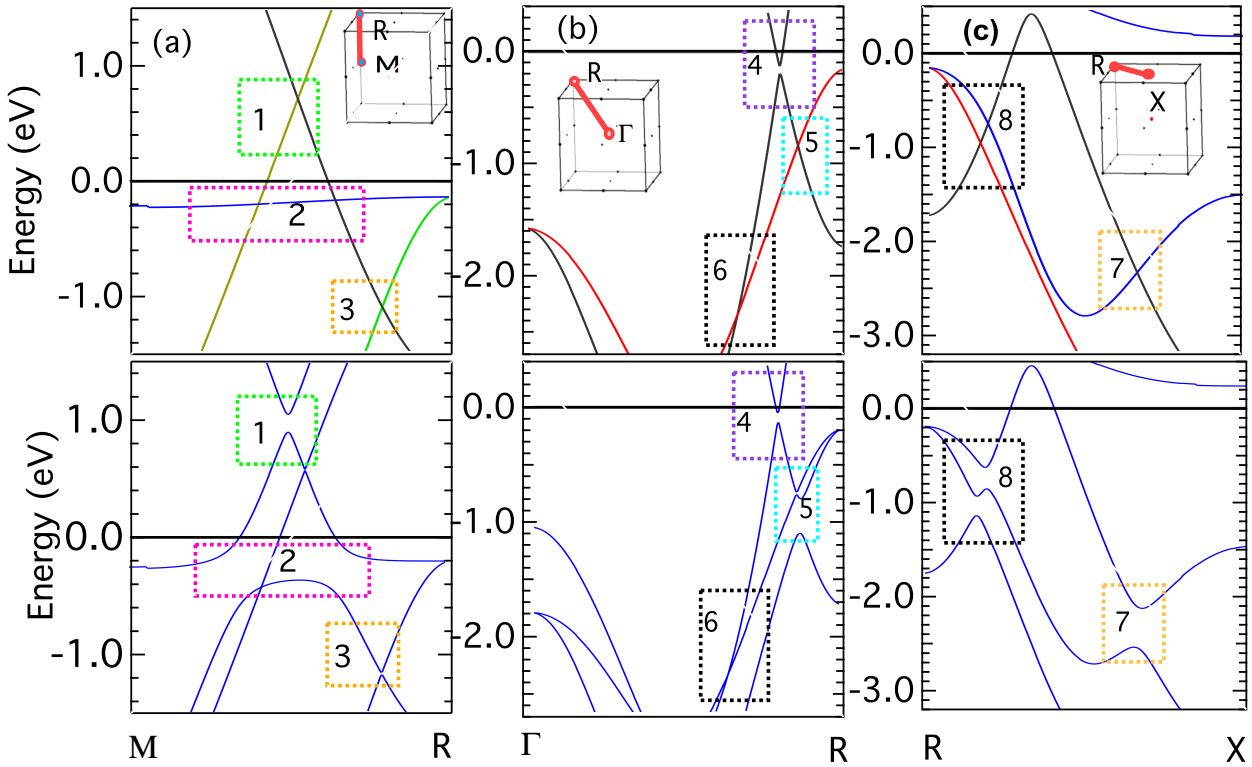

FIGURE 4. (Color online) Zoomed-in version of the electronic band structure of bulk *IrGa* in different segments. Panel (a) top: Calculated zoomed-in irreducible band dispersion around areas 1, 2, and 3 in Fig. 3 along the M-R trajectory is presented with the absence of SO coupling. Panel (a) bottom: The same as panel (a) top but with the presence of SO coupling. Panel (b) top: Calculated zoomed-in irreducible band dispersion around 4, 5, and 6 labels in Fig. 3 shown along k-path Γ-R in the absence of SO coupling. Panel (b) bottom: The same as panel (a) top but in the presence of SO coupling. Panel (c) top: Calculated zoomed-in irreducible band dispersion around the 7 and 8 labels in Fig. 3 shown along k-path R-X in the absence of SO coupling. Panel (c) bottom: The same as panel (c) top but in the presence of SO coupling. The insets on panel (a), (b), and, (c) denote the selected M-R, Γ-R, and R-X paths. Zero energy is set to the Fermi level in all panels.

The dicussion will be continued in both the M-R-X and Γ-R-X planes and recognized as a three-dimensional nodal line around R related to the labeling boxes 3, 5, and 8 together in Fig. 3, with and without SO coupling.

Moving into the Γ-R trajectory, the zoomed-in picture in Fig. 4 shows that there is an avoided-crossing marked in bin 4. The gap is barely sensitive to the SO effect. The gap with the absence of SO as shown in the top panel of Fig. 4(b) is protected by the C_{3v} space group and is located at the coordinates $(-0.43905, 0.43905, 0.43905)$ with band index Γ_1. We freeze the discussion of this feature due to the same symmetries of the bands shown in irreducible representation. Bin 5 in Fig. 4 is related to the end of the nodal line predicted around the R point in Γ-R. A crossing point at the coordinates $(-0.46948, 0.46948, 0.46948)$ with band indices Γ_1 and Γ_3 is protected by the absence of the SO effect and falls along the threefold rotation axis with symmetry C_{3v}. With inclusion the SO gap is opened with threefold degeneracy which is dominated by crossing of *Ga*-s orbitals and *Ir*-deg orbitals. Additionally, bin 6 (-2.2 eV) at coordinates $(-0.36565, 0.36565, 0.36565)$ in Fig. 4 displays a linear band (Γ_1 and Γ_3) crossing with space group symmetry C_{3v}, which is protected by inclusion of SO coupling but band index Γ_1 is separated.

Box 8 shows a zoomed-in picture of the R-X ($k_x = k_z$ and $k_y = \pi/a$) plane shown in Fig. 4(c), representing the end of the nodal line located around R. One crossing is located at an energy of -0.95 eV with coordinates $(-0.46219, 0.55342, -0.46219)$ and band indices Γ_1 and Γ_3 with the space group symmetry of C_{2v}. The other crosses at an energy of -0.74 eV with coordinates $(-0.44395, 0.55342, -0.44395)$ and indices Γ_1 and Γ_3 of space group symmetry C_{2v}. They are dominated with *Ga*-s orbitals and *Ir*-deg orbitals and split into three bands with SO included as displayed in Fig. 4(c).

Additionally, a Dirac crossing (mainly from *Ir*-dt2g orbitals) indicated in bin 7 at energy -2.33 eV with coordinates $(-0.18853, 0.55342, -0.18853)$, and bands indices Γ_1 and Γ_2 protected by symmetry C_{2v} open up the gap with the presence of the SO effect. With the discussion of bins 8-7 together, it is a nodal line protected by the absence of SO effect and transits into a topological insulator state with the band inversion by inclusion of SO coupling. Recent

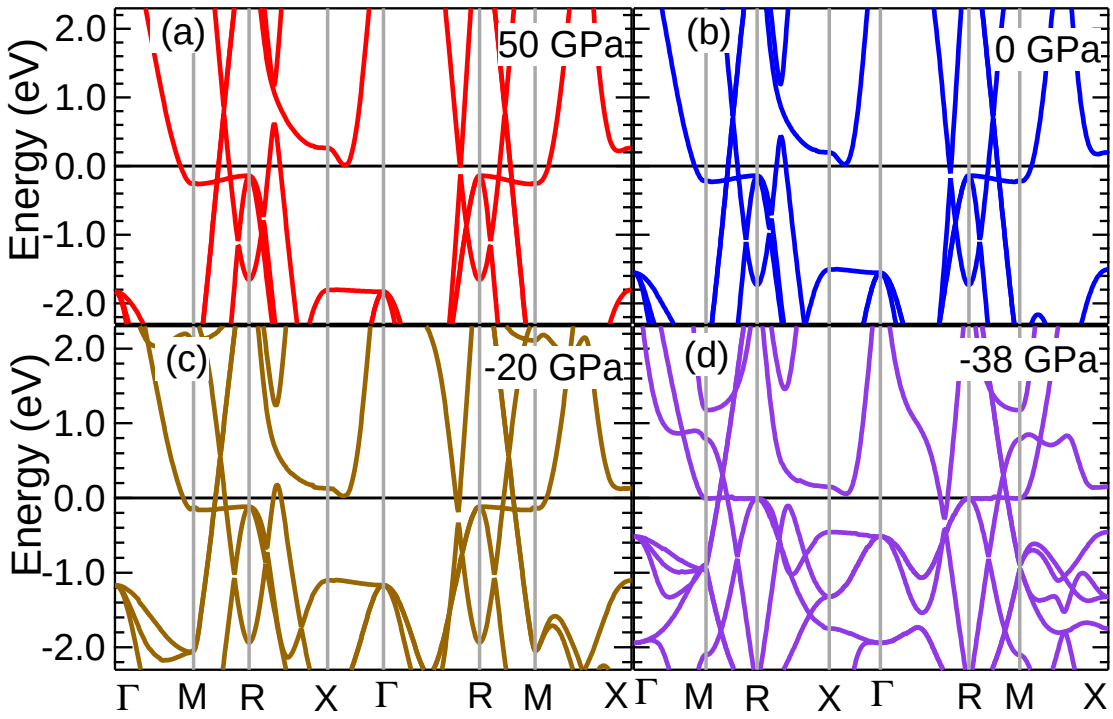

FIGURE 5. Band structure of bulk *IrGa* under four pressure values. Panel (a): Evolution of bulk band dispersion along high symmetric k-path Γ-M-R-X-Γ-R-M-X, the same path used in Fig. 3 for pressure 50 GPa. Panel (b): The same as panel (a) but for pressure 0 GPa. Panel (c): The same as panel (a) but for pressure -20 GPa. Panel (d): The same as panel (a) but for critical pressure -38 GPa.

studies predicted trivial phase transitions into a topological insulator by applying physical pressure [66-69]. To study the topological phases under pressure, volume optimization is performed and the lattice parameter related to applied physical pressure is obtained. The band structure of *IrGa* was calculated for both compressive and tensile stress as shown in Fig. 5. The left panel displays the calculated bulk band structure for pressure 50 GPa (a = 2.8891), and the top right panel indicates the same for 0 GPa (a = 3.0566). There is no impressive effect to the band structure except that the band structure is stretched out more around the Fermi energy. The bottom left panel displays the band structure for -20 GPa (a = 3.2006) with the significant differences upon 0 G Pa. All the labeling from bins 1-8 have substantial swaps in the energy scale for this particular pressure. Hence, we decide to tune the band structure with tensile stress and originate the critical pressure as -38 GPa (a = 3.6594), which brings the flat band in the M-R plane to the Fermi level as shown in the bottom right panel of Fig. 5. A zoomed-in picture of this behavior is displaced in Fig. 6. Figure 6(a) denotes the irreducible representation of band structure in the M-R-X plane for pressure -38 GPa, which shows a closer look of swaps of energy scales due to physical pressure. In this critical pressure, the predicted Dirac point in bin 1 is lowered to 0.3 eV, whereas the flat band is pulled to 0 eV. Although the nodal line around R is broadened out from the Fermi level, in Fig. 6 boxes 7 and 8 band inversion is rendered closer to the Fermi level than they appeared.

Further, there are significant outcomes on total DOS at -38 GPa pressure with SO effect as displayed in Fig. 6(b). It shows that at this critical pressure, both materials will be promising candidates for future studies.

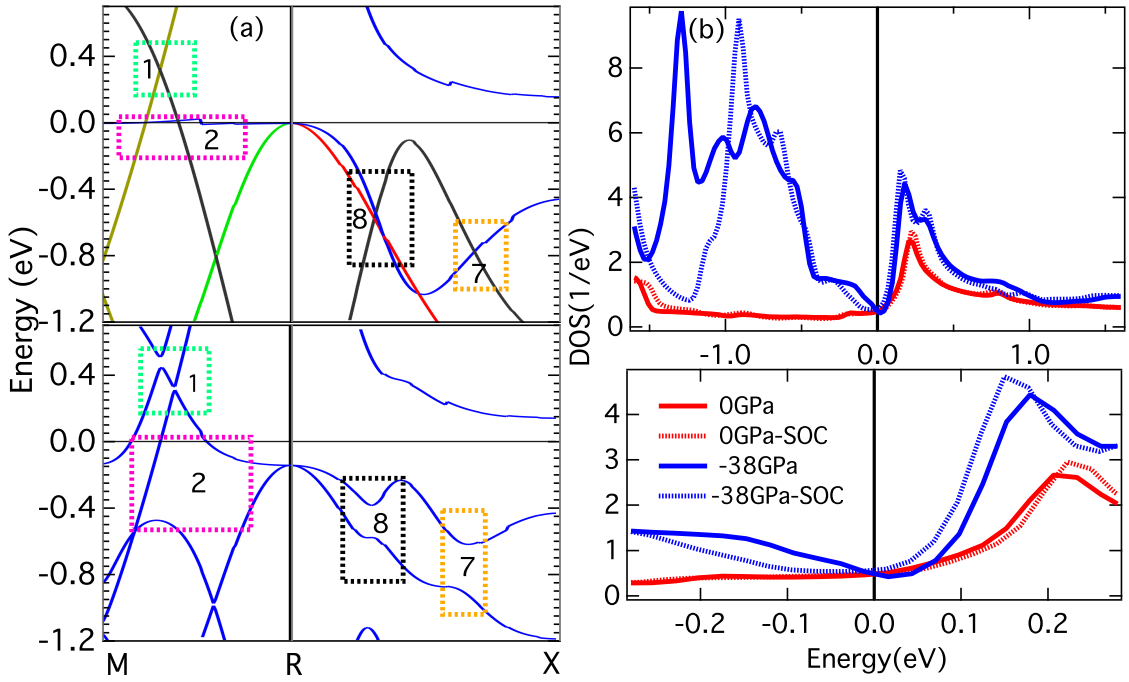

FIGURE 6. Zoomed-in version of the bulk band structure in the M-R-X segment with critical pressure -38 GPa and total DOS for critical pressure -38 GPa. Panel (a) top: Calculated zoomed-in irreducible band dispersion in the M-R-X path for bins 1, 2, 7, and 8 in Fig. 3. Panel (a) bottom: The same as panel (a) top but in the presence of SO coupling for pressure -38 GPa. Panel (b) top: Corresponding total DOS of *IrGa* for pressure zero and -38 GPa are displayed. The red solid line indicates the total DOS in zero pressure, whereas the blue solid line denotes the same for a critical pressure of -38 GPa. Similarly, the corresponding colored dotted lines show the total DOS for the SO effect for zero and critical pressure, respectively. Panel (b) bottom displays the zoomed-in DOS near the Fermi level. The solid black line at zero indicates the Fermi level.

CONCLUSION

In summary, our studies of *IrGa* and *RhGa* compounds suggest that both are important systems to study due to the unusual behavior of bands near the Fermi level and strong spin-orbit coupling effect. Since Dirac material has theoretical and experimental academic significance, further studies of *IrGa* and *RhGa* are suggested. Most importantly, we predict drastically different topological properties near the Fermi energy with significantly different behaviors of band crossings and touchings. A linear band crossing near the Fermi level was discovered, and Dirac points, nodal lines, and flat bands with tremendously distinct actions were predicted. The SO calculations indicate the degeneracy with band inversions. The predicted unusual electronic structure of *IrGa* and its important topological properties will be useful for searching for novel Dirac fermions and materials for further studies.

ACKNOWLEDGMENTS

D. G., J. P. A., and N. H. acknowledge financial support from a STEMatics grant, Department of Education. N. H. and K. H. acknowledge the Extreme Science and Engineering Discovery Environment (XSEDE), supported by grant number TG-PHY190050.

REFERENCES

1. M. Z. Hasan and C. L. Kane, Rev. Mod. Phys. **82**, 3045 (2010).
2. X. L. Qi, and S. C. Zhang, Rev. Mod. Phys. **83**, 1057 (2011).
3. B. J. Yang and N. Nagaosa, Nat. Commun. **5**, 4898 (2014)
4. G. Xu, H. Weng, Z. Wang, X. Dai, and Z. Fang, Phys. Rev. Lett. **107**, 186806 (2011).
5. A. A. Zyuzin, S. Wu, and A. A. Burkov, Phys. Rev. B. **85**, 165110 (2012).
6. R. R Nair, P. Blake, A. N. Grigorenko, K. S. Novoselov, T. J. Booth, T. Stauber, N. M. R. Peres, and A. K. Geim, Science **320**, 1308–1308 (2008).
7. Y. Zhang, Y. W. Tan, H. L. Stormer, and P. Kim, Nature, **438**, 201-202 (2005).
8. Z. K. Liu, J. Jiang, B. Zhou, Z. J. Wang, H. M. Weng, D. Prabhakaran, S-K. Mo, H. Peng, P. Dudin, T. Kim, M. Hoesch, Z. Fang, X. Dai, Z. Shen, D. L. Feng, Z. Hussain, and Y. L. Chen, Nat. Mater. **13**, 677-681 (2014).
9. Yu Rui, H. Weng, Z. Fang, X. Dai, and X. Hu, Phys. Rev. Lett. **115**, 036087 (2015).
10. S. M. Young, S. Zaheer, J. C. Y. Teo, C. L. Kane, E. J. Mele, and A. M. Rappe, Phys. Rev. Lett. **108**, 140405 (2012).
11. H. Huang, S. Zhou, and W. Duan, Phys. Rev. B **94**, 121117 (2016).
12. L. Muechler, A. Alexandradinata, Titus Neupert, and R. Car, Phys. Rev. X **6**, 041069 (2016).
13. Y. Chen, Y. Xie, S. A. Yang, H. Pan, F. Zhang, M. Cohen, and S. Zhang, Nano Lett. **15**, 6974-8 (2015).
14. Z. K. Liu, Y. Zhang, Z. J. Wang, H. M. Weng, D. Prabhakaran, S-K. Mo, Z. X. Shen, Z. Fang, X. Dai, Z. Hussain, and Y. L. Chen, Science, **343**, 864-7 (2014).
15. M. Neupane, S-Y. Xu, R. Sankar, N. Alidoust, G. Bian, C. Liu, I. Belopolski, T-R. Chang, H-T. Jeng, H. Lin, A. Bansil, F. Chou, and M. Z. Hasan, Nat. Commun. **5**, 3786 (2014).
16. M. Yan, H. Huang, K. Zhang, E. Wang, W. Yao, K. Deng, G. Wan, H. Zhang, M Arita, H. Yang, Z. Sun, H. Yao, Y. Wu, S. Fan, W. Duan, and S. Zhou, Nat. Commun. **8**, 257 (2017).
17. H.-J. Noh, J. Jeong, E-J. Cho, K. Kim, B. I. Min, and B-G. Park, Phys. Rev. Lett. **119**, 016401 (2017).
18. Q. D. Gibson, L. M. Schoop, L. Muechler, L. S. Xie, M. Hirschberger, N. P. Ong, R. Car, and R. J. Cava, Phys. Rev. B. **91**, 205128 (2015).
19. L. M. Schoop, F. Pielnhofer, and B. Lotsch, Chem. Mater. **30**, 3155-3176 (2018).
20. T. Liang, Q. Gibon, M. N. Ali, M. Liu, R. J. Cava, and N. P. Ong, Nat. Mater. **14**, 280-284 (2015).
21. P. Hořava, Phys. Rev. Lett. **95**, 016405 (2005).
22. H. Weng, Y. Liang, Q. Xu, R. Yu, Z. Fang, X. Dai, and Y. Kawazoe, Phys. Rev. B **92**, 045108 (2015).
23. L. S. Xie, L. M. Schoop, E. M. Seibel, Q. D. Gibson, W. Xie, and R. J. Cava, APL Mater., **3**, 083602 (2015).
24. Q. Xu, R. Yu, Z, Fang, and X. Dai, Phys. Rev. B **95**, 045136 (2017).
25. Z. Wang and G. Wang, Phys. Lett. A **381**, 2856-2859 (2017).
26. A. Yamakage, Y. Yamakawa, Y. Tanaka, and Y. Okamoto, J. Phys. Soc. Jpn. **85**, 013708 (2016).
27. X. Feng, C. Yue, Z. Song, Q. Wu, and B. Win, Phys. Rev. Mater. **2**, 014202 (2018).
28. M. Hirayama, R. Okugawa, T. Miyake, and S. Murakami, Nat. Commun. **8**, 14022 (2017).
29. G. P. Mikitik and Y. Sharlai, Phys. Rev. B **73**, 235112 (2006).
30. H. Huang, J. Liu, D. Vanderbilt, and W. Duan, Phys. Rev. B **93**, 201114 (2016).
31. J. Howard, J. Steier, N. Haldolaarchchige, and K. Hettiarachchilage, J **4,** 577-588 (2021).
32. S.-M. Huang, S.-Y. Xu, I. Belopolski, C.-C. Lee, G. Chang, B. Wang, N. Alidoust, G. Bian, M. Neupane, C. Zhang, S. Jia, A. Bansil, H. Lin, and M. Z. Hasan, Nat. Commun. **6**, 7373 (2015).
33. R. Lou, J.-Z. Ma, Q.-N. Xu, B.-B. Fu, L.-Y. Kong, Y.-G. Shi, P. Richard, H.-M. Weng, Z. Fang, S.-S. Sun, Q. Wang, H.-C. Lei, T. Qian, H. Ding, and S.-C. Wang, Phys. Rev. B **93**, 241104 (2016).
34. D. Takane, Z. Wang, S. Souma, K. Nakayama, C. X. Trang, T. Sato, T. Takahashi, and Yoichi Ando, Phys. Rev. B **94**, 121108 (2016).
35. Y. Wu, L.-L. Wang, E. Mun, D. D. Johnson, D. Mou, L. Huang, Y. Lee, S. L. Bud'ko, P. C. Canfield, and A. Kaminski, Nat. Phys **12**, 667-671 (2016).
36. G. Bian, T.-R. Chang, R. Sankar, S.-Y. Xu, H. Zheng, T. Neupert, C.-K. Chiu, S.-M. Huang, G. Chang, I. Belopolski, D. S. Sanchez, M. Neupane, N. Alidoust, C. Liu, B. Wang, C.-C. Lee, H.-T. Jeng, C. Zhang, Z. Yuan, S. Jia, A. Bansil, F. Chou, H. Lin, and M. Z. Hasan, Nat. Commun. **7**, 105556 (2016).
37. A. Topp, J. M. Lippmann, A. Varykhalov, V. Duppel, B. V. Lotsch, C. R. Ast, and Leslie M. Schoop, New J. Phys. **18**, 125014 (2016).
38. E. Haubold, K. Koepernik, D. Efremov, S. Khim, A. Fedorov, Y. Kushnirenko, J. van den Brink, S. Wurmehl, B. Büchner, T. K. Kim, M. Hoesch, K. Sumida, K. Taguchi, T. Yoshikawa, A. Kimura, T. Okuda, and S. V. Borisenko, Phys. Rev. B **95**, 241108(R) (2017).
39. L. M. Schoop, M. N. Ali, C. Straßer, A. Topp, A. Varykhalov, D. Marchenko, V. Duppel, S. S. P. Parkin, B. V. Lotsch, and C. R. Ast, Nat. Commun. **7**, 11696 (2016).
40. J. Hu, Z. Tang, J. Liu, X. Liu, Y. Zhu, D. Graf, K. Myhro, S. Tran, C. N. Lau, J. Wei, and Z. Mao, Phys. Rev. Lett. **117**, 016602 (2016).
41. S.-Y. Xu, I. Belopolski, N. Alidoust, M. Neupane, G. Bian, C. Zhang, R. Sankar, G. Chang, Z. Yuan, C.-C. Lee, S.-M. Huang, H. Zheng, J. Ma, D. Sanchez, B. Wang, A. Bansil, F. Chou, P. P. Shibayev, H. Lin, S. Jia, and M. Z. Hassan, Science **349**, 613-617 (2015).
42. B. Q. Lv, N. Xu, H. M. Weng, J. Z. Ma, P. Richard, X. C. Huang, L. X. Zhao, G. F. Chen, C. E. Matt, F. Bisti, V. N. Strocov, J. Mesot, Z. Fang, X. Dai, T. Qian, M. Shi, and H. Ding, Nat. Phys. **11**, 724-727 (2015).
43. A. A. Soluyanov, D. Gresch, Z. Wang, Q. Wu, M. Troyer, X. Dai, and B. A. Bernevig, Nature **527**, 495-498 (2015).
44. K. Deng, G. Wan, P. Deng, K. Zhang, S. Ding, E. Wang, M. Yan, H. Huang, H. Zhang, Z. Xu, J. Denlinger, A. Fedorov, H. Yang, W. Duan, H. Yao, Y. Wu, S. Fan, H. Zhang, X. Chen, and S. Zhou, Nat. Phys. **12**, 1105-1110 (2016).
45. N. Xu, H. M. Weng, B. Q. Lv, C. E. Matt, J. Park, F. Bisti, V. N. Strocov, D. Gawryluk, E. Pomjakushina, K. Conder, N. C. Plumb, M. Radovic, G. Autès, O. V. Yazyev, Z. Fang, X. Dai, T. Qian, J. Mesot, H. Ding, and M. Shi, Nat. Commun. **7**, 11006 (2016).
46. L. Yang, Z. Liu, Y. Sun, H. Peng, H. Yang, T. Zhang, B. Zhou, Yi.Zhang, Y. Guo, M. Rahn, D. Prabhakaran, Z. Hussain, S.-K. Mo, C. Felser, B. Yan, and Y. Chen, Nat. Phys. **11**, 728-732 (2015).
47. T.-R. Chang, S.-Y. Xu, D. S. Sanchez, W.-F. Tsai, S.-M. Huang, G. Chang, C.-H. Hsu, G. Bian, I. Belopolski, Z.-M. Yu, S. A. Yang, T. Neupert, H.-T. Jeng, H. Lin, and M. Z. Hasan, Phys. Rev. Lett. **119**, 026404 (2017).

48. G. B. Halàsz and L. Balents, Phys. Rev. B. **85**, 035103 (2012).
49. P. Hohenberg and W. Kohn, Phys. Rev. **136**, B864 (1964).
50. W. Kohn and L. J. Sham, Phys. Rev. **140**, A1133 (1965).
51. C. Kittle, *Introduction to Solid State Physics*, 8th ed. (John Wiley & Sons, NY, 2004), pp. 1-704.
52. G. F. Koster, J. D. Dimmock, R. G. Wheeler, and H. Statz, *Properties of the Thirty-Two Point Groups*, 1st ed. (MIT Press, Cambridge, MA, 1963), pp. 1-104.53.
53. K. J. Schulz, O. A. Musbah, and Y. A. Chang, et al., Bull. Alloy Phase Diagrams **11**, No. 3, 211-215 (1990).
54. N. Arikan, Z. Charifi, H. Baaziz, H. Unver, and G. Ugar, Phys. Chem. Solids **77**, 126-132 (2015).
55. K. J. Schulz, O. Musbah, and Y. Chang, J. Phase Equilib. **12**, 10-14 (1991).
56. P. Blaha, K. Schwarz, P. Sorantin, and S. B. Trickey, Commput. Phys. Commun. **59**, 399–68. (1990).
57. P. Blaha, K. Schwarz, F. Tran, R. Laskowski, G. K. H. Madsen, and L. D. Marks, J. Chem. Phys. **152**, 074101 (2020).
58. J. P. Perdew, K. Burke, and M. Ernzerhof, Phys. Rev. Lett. **77**, 3865 (1996).
59. D. J. Singh,et al., *Planewaves, Pseudopotentials, and the LAPW Method*, 2nd ed. (Springer, New York, 1996).
60. G. K. H. Madsen, P. Blaha, K. Schwarz, E. Sjostedt, and L. Nordstrom, Phys. Rev. B **64**, 195134 (2001).
61. A. A. Burkov, M. D. Hook, and Leon Balents, Phys. Rev. B **84**, 235126 (2011).
62. A. S. Cuamba, H.-Y. Lu, L. Hao, and C. S. Ting, preprint arXiv:1801.01113 [cond-mat.mtrlsci] (2018).
63. N. B. Kopnin, T. T. Heikkila, and G. E. Volovik, Phys. Rev. B **83**, 220503 (2011).
64. D. Leykam, A. Andreanov, and S. Flach, Adv. Phys.: X **3**, 1473052 (2018).
65. N. Ehlen, M. Hell, G. Marini, E. H. Hasdeo, R. Saito, Y. Falke, M. O. Goerbig, G. Di Santo, L. Petaccia, G. Profeta, and A. Grüneis, ACS Nano **14**, 1055-1069 (2020).
66. M. S. Bahramy, P. D. C. King, A. de la Torre, J. Chang, M. Shi, L. Patthey, G. Balakrishnan, Ph. Hofmann, R. Arita, N. Nagaosa, and F. Baumberger, Nat. Commun. **3**, 679 (2012).
67. M. S. Bahramy, B.-J. Yang, R. Arita, and N. Nagaosa, Nat. Commun. **3**, 679 (2012).
68. M. Hirayama, R. Okugawa, S. Ishibashi, S. Murakami, and T. Miyake, Phys. Rev. Lett. **114**, 206401 (2015).
69. H. Gao and W. Ren, Carbon **158**, 210-215 (2020).